ACS APPLIED ELECTRONIC MATERIALS

pubs.acs.org/acsaelm

Article

Transition from Nonpolarizable to Polarizable Regime in Ag/AgCl-Gated Electrochemical Devices

Renan Colucci,* Paula Cristina Rodrigues, Rafael Francisco Santiago de Souza, and Gregório Couto Faria*

Cite This: *ACS Appl. Electron. Mater.* 2025, 7, 10998−11005

Read Online

ACCESS | Metrics & More | Article Recommendations | Supporting Information

ABSTRACT: Organic mixed conductors (OMCs) are of great interest for a variety of electrochemical device applications because of their ability to support both ionic and electronic transport. Device operation relies on ion accumulation from the electrolyte within the bulk of the OMC, yielding a capacitance that scales with the film volume. However, this volume-dependent capacitance has been reported to hold only within limited ranges of voltage and film thickness, constraining device performance. Here, we investigate the origin of this limitation and its correlation with the Ag/AgCl-doping electrode properties. To this end, we fabricated capacitor-like devices based on poly(3,4-ethylenedioxythiophene):poly(styrenesulfonate) (PEDOT:PSS) with constant surface area and varying film thicknesses, employing commonly used nonpolarizable Ag/AgCl pellets as doping electrodes. Our results show that the breakdown of the linear capacitance−volume relationship arises from an increasing voltage drop at the Ag/AgCl−electrolyte interface. According to the Butler−Volmer equation, electrochemical reactions at a nonpolarizable electrode surface proceed at a finite rate. When the current demand surpasses this rate, the electrode can no longer behave ideally, resulting in increased charge-transfer resistance and accumulation of charge at the interface, resulting in a transition toward polarizable-like behavior. This transition is marked by the growing voltage drop at the Ag/AgCl−electrolyte interface, which reduces the effective channel voltage and, consequently, the capacitance of the OMC. These electrical findings were corroborated by depth-profile X-ray photoelectron spectroscopy (XPS), which revealed a significant decrease in the cation concentration with depth. Overall, this study underscores the critical role of doping electrode properties in the design and optimization of OMC-based electrochemical devices.

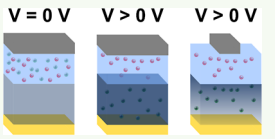

KEYWORDS: *OMC, PEDOT:PSS, capacitor-like device, volumetric capacitance, nonpolarizable electrode*

INTRODUCTION

Organic mixed conductors (OMCs) are materials capable of efficiently supporting both ionic and electronic transport.[1−4] When in contact with an electrolyte, ions can permeate the bulk of the OMC under an applied voltage, leading to electrochemical interactions that modify the film's electrical, optical, and morphological properties.[5] This ion uptake depends on the OMC volume, giving rise to the so-called volumetric capacitance (C*).[6,7] Owing to this property, OMC-based electrochemical devices function as highly efficient ion-to-electron transducers. For instance, organic electrochemical transistors (OECTs) can achieve ion−electron transconductance values of tens of millisiemens, whereas electrolyte-gated organic field-effect transistors (EGOFETs), where ions accumulate primarily at the electrolyte−polymer interface, reach maximum transconductance in the microsiemens range.[8,9]

Although widely accepted, the linear relationship between capacitance and film volume has its limitations.[10,11] For poly(3,4-ethylenedioxythiophene):poly(styrenesulfonate) (PEDOT:PSS) films, this linear dependence holds only up to a critical volume (~10^6 μm^3). Beyond this threshold, the capacitance plateaus, indicating that further increases in volume do not yield additional charge storage. The origin of this breakdown is not yet fully understood, but several hypotheses have been proposed, including incomplete film hydration, intrinsically inaccessible regions within the film, electrostatic screening by nearby ions, compositional inhomogeneities, and energy disorder in ion-binding sites.[7,10,11]

However, limitations in volumetric charging must also be considered in the broader context of device architecture, particularly regarding the doping electrode. The efficiency of electrochemical devices, such as OECTs, depends strongly on the type of gate electrode used.[12,13] Polarizable electrodes, such as gold (Au) and platinum (Pt), form a double-layer capacitor at the gate/electrolyte interface.[14] This interfacial capacitance divides the applied voltage via its capacitive reactance, effectively reducing the voltage across the electrolyte/channel interface and lowering the overall device capacitance. To minimize this gate-electrode bottleneck, the gate capacitance must be substantially larger than the channel

Received: September 5, 2025
Revised: December 5, 2025
Accepted: December 8, 2025
Published: December 13, 2025

capacitance. In contrast, nonpolarizable electrodes, such as Ag/AgCl pellets, operate in a Faradaic regime.[14] In this case, the voltage drop at the gate/electrolyte interface is minimal due to negligible charge-transfer resistance,[15] enabling more efficient gating and improved device performance. When properly implemented, nonpolarizable gating prevents charge accumulation at the gate/electrolyte interface. For Ag/AgCl electrodes, ions are instead neutralized according to the following electrochemical reaction, rather than accumulating at the interface

$$\mathrm{Ag(s) + Cl^-(aq) \leftrightarrow AgCl(s) + e^-} \quad (1)$$

Here, silver (Ag) reacts with chloride ions (Cl^-) in solution to form solid silver chloride (AgCl) while releasing an electron (e^-). It is worth noting that, according to the Butler–Volmer equation,[16,17] the current through a nonpolarizable electrode scale with its surface area (A), as shown in eq 2 below, and depends on the kinetic constant of the electrochemical reaction.[16]

$$I = -nFAk_{0(f)}a_{ox}\exp\left(-\frac{\alpha_c F\chi}{RT}\right) + nFAk_{0(b)}a_{red}\exp\left(\frac{+\alpha_a F\chi}{RT}\right) \quad (2)$$

where I is the net electrical current, n is the stoichiometric number of electrons transferred during the process, F is the Faraday constant, A is the electrode area, R is the ideal gas constant, and T is the temperature. The constants $k_{0(f)}$ and $k_{0(b)}$ are the standard heterogeneous rate constants for the forward and backward reactions, in units of $m.s^{-1}$. The terms α_{ox} and α_{red} are, respectively, the number of activities of the oxidized and reduced species, with units of $mol.m^{-3}$. The terms α_c and α_a are the transfer coefficients of the forward (cathodic) and backward (anodic) half-reactions, respectively. Parameter χ (chi) is the overpotential measured relative to the standard balance potential, as shown below

$$\chi = E_f - E_{bp(0)} \quad (3)$$

where E_f is the Fermi potential and $E_{bp(0)}$ is the standard balance potential.

From eq 2, the current through a nonpolarizable electrode is inherently limited by its surface area, which determines the number of available sites for charge-transfer (as described in eq 1). In electrochemical devices with low capacitance, the charge-transfer process at a standard Ag/AgCl pellet typically meets the ionic demand. In these cases, the reaction kinetics are sufficiently fast to neutralize the necessary ions without limiting current throughput. However, in devices with higher capacitances, the situation becomes more complex. As the film volume increases, more ions must be neutralized at the gate electrode to sustain the device current. Depending on the electrode area, the Ag/AgCl electrode may be unable to efficiently neutralize ions, increasing charge-transfer resistance and causing ion accumulation at the gate. This results in a voltage drop at the gate/electrolyte interface, creating behavior analogous to that of a polarizable electrode.[16,18]

Here, we investigate the origins of volumetric capacitance limitations in PEDOT:PSS films and their correlation with the choice of doping electrode. To this end, we fabricated capacitor-like devices with a constant surface area of 1.43 cm^2 and film thicknesses ranging from 100 to 2500 nm. To evaluate the effect of the doping electrode, two nonpolarizable electrodes with different film-to-electrode surface area ratios (1.4 and 18) were employed. The devices were characterized using transient measurements, and the experimental data were analyzed using the Faria–Duong (F&D) model.[19] Furthermore, morphological characterization was performed via depth-profile X-ray photoelectron spectroscopy (XPS) to examine ion distribution across the film thickness. By inducing a transition from nonpolarizable to polarizable behavior in the doping electrode, we show that the Ag/AgCl surface area must be carefully chosen to match the properties of the OMC film and electrolyte in order to preserve nonpolarizable behavior. These findings provide critical insights into the factors governing volumetric capacitance in OMCs and highlight the limitations of standard Ag/AgCl pellets commonly used in electrochemical device fabrication.

EXPERIMENTAL SECTION

Materials. 4-Dodecylbenzenesulfonic acid (DBSA), ethylene glycol, (3-glycidyloxypropyl)trimethoxysilane (GOPS), potassium chloride (KCl), and magnesium chloride ($MgCl_2$) were purchased from Sigma-Aldrich Co. Poly(3,4-ethylenedioxythiophene):polystyrenesulfonate (PEDOT:PSS) aqueous solution (Clevios PH1000) was obtained from Heraeus Ltd. The pellets used were obtained from Harvard Apparatus. Small doping electrode: code E200, with diameter 1.5 mm and 3 mm thick; and Big doping electrode: code E204, with diameter 12.5 mm and 1 mm thick.

Device Fabrication. Glass slides were cut into dimensions of 1.5 cm × 1.5 cm. The slides were initially washed with soap and water, followed by ultrasonic cleaning for 15 min at 60 °C in a soap-to-water solution (1:10 v/v). Subsequently, the slides were rinsed with ultrapure water and subjected to a second ultrasonic cleaning for 15 min at 60 °C in ultrapure water. The substrates were then immersed in isopropanol and ultrasonicated for 15 min at 60 °C. Finally, the slides were dried under a nitrogen stream and exposed to UV light for 10 min. The cleaned glass slides were coated with a 10 nm chromium layer followed by a 100 nm gold layer. The deposition was performed by resistive thermal evaporation under a pressure of 10^{-5} bar, at a deposition rate of 3 Å/s. The source temperatures were 1560 °C for chromium and 1063 °C for gold.

The active layer was prepared using a PEDOT:PSS (Clevios PH1000) solution, modified with 5% v/v ethylene glycol, 1% v/v GOPS, and 0.1% v/v DBSA. Specifically, 19 mL of PEDOT:PSS was transferred into a clean vial, followed by the sequential addition of 1 mL of ethylene glycol, 200 μL of GOPS, and one drop of DBSA. The mixture was then sonicated at 24 °C for 20 min in an ultrasonic bath to ensure homogeneity. Films were deposited via spin-coating at speeds ranging from 1500 to 300 rpm for 1 min, with thickness controlled by multiple sequential layers as needed. Between each deposition, substrates were annealed at 90 °C for 1 min. After the final layer, films were annealed at 120 °C for 20 min and then immersed in Milli-Q water for 24 h to remove residual low-molecular-weight compounds.[20]

The active layer was defined as the region of the PEDOT:PSS film in contact with the electrolyte. To prevent direct contact between the electrolyte and the contact needle, a 0.4 mm-wide tape barrier was applied (Figure S1). After applying the tape, the dimensions of the exposed area were measured using a caliper, yielding an average active area of (1.43 ± 0.05) cm^2. The electrolyte volume used was 0.250 mL.

Film thicknesses were measured using a Veeco Dektak 150 stylus profilometer. A narrow scratch was made on the film using a steel punch to expose the gold surface. Scans were performed across the film–scratch interface, and the film thickness was determined from the average height difference between the intact film surface and the exposed substrate (Figure S2). Measurements were taken at three different positions on each sample, and the reported thickness corresponds to the mean value, with the error estimated as the standard deviation.

Electrical Measurement. Electrical characterization was performed using a Keithley 2636B source meter, controlled via custom

https://doi.org/10.1021/acsaelm.5c01861
ACS Appl. Electron. Mater. 2025, 7, 10998–11005

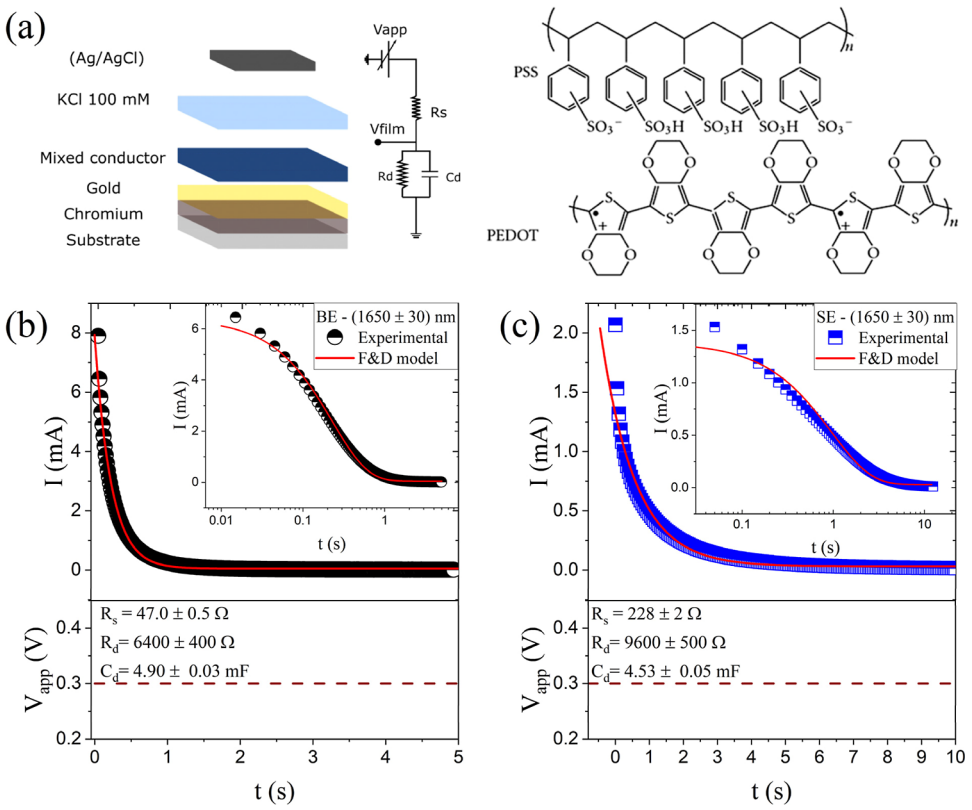

Figure 1. (a) Schematic of the capacitor-like device, equivalent circuit proposed by the F&D model, and the chemical structure of PEDOT:PSS. (b,c) Transient measurements (current vs time under a fixed voltage) for a device with a thickness of (1650 ± 30) nm using BE and SE, respectively. A voltage of 0.3 V was applied to the doping electrode. The red lines represent the fits obtained using the F&D model. Insets display the data on a logarithmic scale to better visualize the agreement between the experimental results and model. The measurements were conducted using a KCl solution with a concentration of 100 mM as the electrolyte. R.Square: BE = 0.99461 and SE = 0.98406.

Python code. Transient measurement was employed, applying a constant voltage of +0.3 V to the doping electrode and recording the resulting current over time. Before measurement, each film underwent a preconditioning cycle[21] involving a series of square voltage pulses from 0.1 to 0.5 V with a step of 0.1 V. This sequence was repeated five times. After four cycles, the electrical response stabilized, indicating that a reproducible operation had been achieved (see Figure S3).

The transient current was analyzed using the Faria−Duong (F&D) model,[19] which describes the system with the equivalent circuit shown in Figure 1a. The model provides estimates of the electrolyte resistance (R_s), the film charge-transfer resistance (R_d), and the film capacitance (C_d). Additionally, the F&D model defines the voltage drop at the electrolyte/film interface (V_{film}), which is critical for subsequent analyses. The equations describing the ionic current and the voltage across the film as a function of time are

$$I(t) = \frac{V_{app}}{R_d + R_s} - \frac{V_{app}R_d}{R_s(R_d + R_s)} e^{(-R_d+R_s/C_dR_dR_s t)} \quad (4)$$

$$V_{film}(t) = \frac{V_{app}}{R_d + R_s}[1 - e^{(-R_d+R_s/C_dR_dR_s t)}] \quad (5)$$

Depth-Profile X-ray Photoelectron Spectroscopy. Depth-profile XPS measurements were performed using a ScientaOmicron ESCA$^+$ spectrometer equipped with a high-performance hemispherical analyzer (EA 125) and monochromatic Al Kα radiation (hν = 1486.6 eV) as the excitation source. Analyses were conducted under ultrahigh vacuum (UHV) at a pressure of 2×10^{-9} mbar. Energy steps of 0.5 and 0.05 eV were used for survey and high-resolution spectra, respectively. To investigate the penetration profile of ionic species, the sample surface was progressively removed via argon ion-beam etching at a kinetic energy of 3.5 keV. Different sputtering times (0−30 min) were applied, and the corresponding depths were measured using a Veeco Dektak 150 profilometer (see Figure S11). Prior to measurement, the samples were polarized until steady state was reached, after which the electrolyte was removed using a nitrogen gun. This procedure effectively immobilized the ions within the bulk of the film for analysis.

RESULTS AND DISCUSSION

Figure 1a illustrates the architecture of the PEDOT:PSS-based capacitor device used in the transient measurements. All devices had a surface area of (1.43 ± 0.05) cm^2 and thicknesses ranging from 100 to 2000 nm, corresponding to volumes between 1.8×10^7 μm^3 and 2.3×10^8 μm^3. To investigate the effect of the film-to-doping-electrode surface area ratio (A_{film}/A_{Dop}), two nonpolarizable Ag/AgCl pellets with different areas were used as doping electrodes: A_{film}/A_{Dop} = 1.4 (referred to as the "big doping electrode" − BE) and A_{film}/A_{Dop} = 18 (referred to as the "small doping electrode" − SE). An aqueous 100 mM KCl solution was employed as the electrolyte in all experiments, unless otherwise specified.

Electrical characterization was performed using transient measurement, where a square-wave potential is applied to the doping electrode and the resulting current is recorded over time. In its pristine state, PEDOT:PSS is a highly doped p-type semiconductor, with PEDOT chains carrying positive polaronic/bipolaronic charges and PSS acting as the doping ion (Figure 1a).[22] During measurements, a positive voltage of 0.3 V was applied to the doping electrode, causing cations from the electrolyte to penetrate and swell the PEDOT:PSS film. This process screens the PSS anions, depleting the polaronic/

https://doi.org/10.1021/acsaelm.5c01861
ACS Appl. Electron. Mater. 2025, 7, 10998−11005

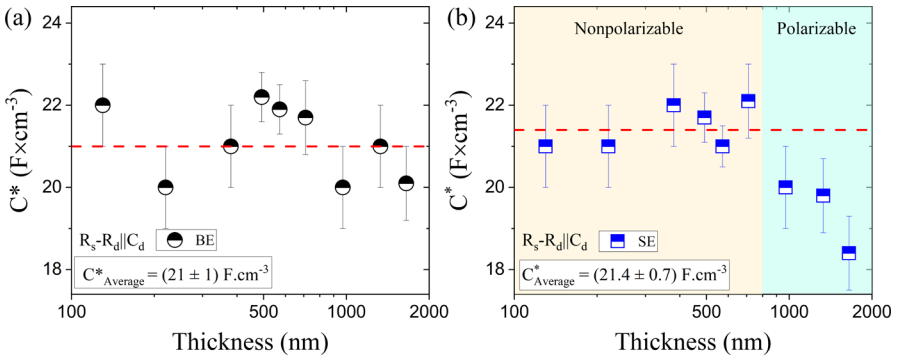

Figure 2. (a,b) Volumetric capacitance of each film versus thickness for the BE and SE, respectively. The dashed line indicates average volumetric capacitance. The background colors in (b) indicates the region where there is the transition from nonpolarizable to polarizable regime. The measurements were performed using a KCl solution as the electrolyte.

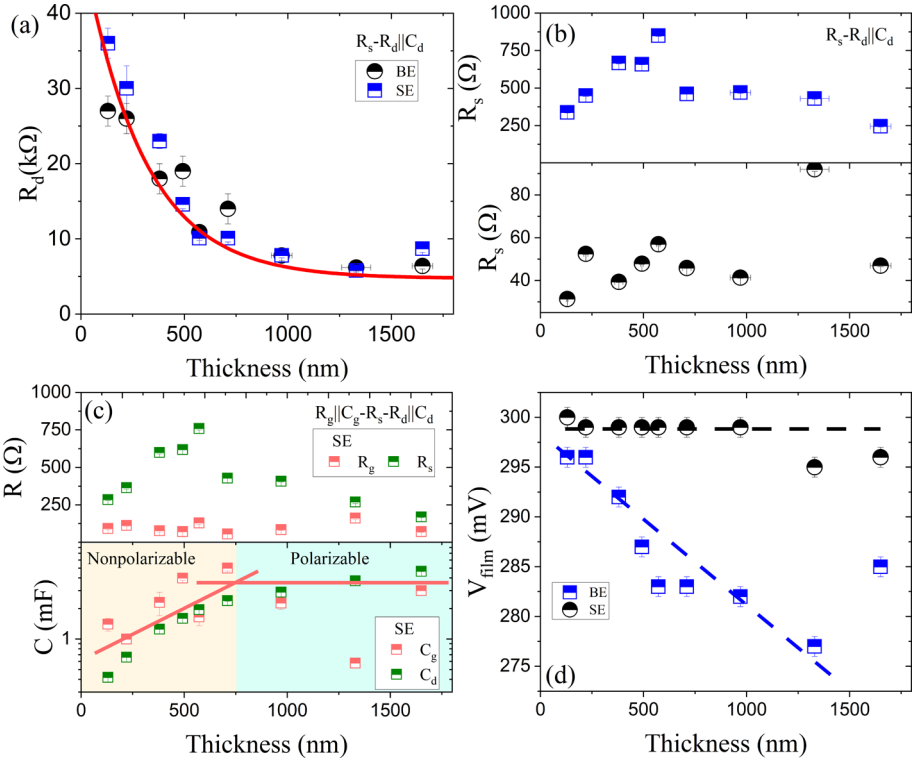

Figure 3. (a,b) Charge transfer resistance (R_d) and electrolyte resistance (R_s) obtained using F&D model for BE and SE (c) Resistances (upper box) and capacitances (bottom box) obtained fitting the date from SE using the equivalent circuit $R_g||C_g - R_s - R_d||C_d$. The background colors in Figure 3c (bottom) indicates the region where there is the transition from nonpolarizable to polarizable regime. The pink line is provided as a guide for the eye. (d) Voltage on the film (V_{film}^{steady}) after reaching the steady state as a function of the film thickness calculated using eq 5 (F&D mode). The measurements were performed using a KCl solution as the electrolyte.

bipolaronic charges and inducing dedoping of the polymer film.

Figure 1b,c present transient measurements for a device with a thickness of (1650 ± 30) nm, analyzed using the BE and SE doping electrodes, respectively. Comparison of the two panels reveals that the device tested with BE exhibits a higher peak current and a faster decay to zero, indicating that the A_{film}/A_{Dop} ratio directly influences both capacitance and system kinetics. To further analyze these results, the transient curves were fitted using the Faria–Duong (F&D) model, which represents the device as an $R_s - R_d||C_d$ equivalent circuit (Figure 1a).[19] Here, R_s denotes the total electrolyte resistance, including possible contributions from charge-transfer resistance and capacitive reactance at the doping electrode/electrolyte interface, R_d represents the charge-transfer resistance in the OMC bulk, and C_d is the film capacitance. The red lines in Figure 1b,c show the F&D model fits, demonstrating excellent agreement with the experimental data. This agreement is particularly clear in the inset, where the time axis is plotted logarithmically to enhance visibility. Fits for the remaining samples are provided in the Supporting Information (Figured S4 and S5, Tables S1 and S2).

The volumetric capacitance corresponding to each measured film was calculated using the capacitance values obtained from the F&D model, taking account the contact area of the PEDOT:PSS film with the electrolyte and the film thickness estimated by profilometry. For BE, the average volumetric capacitance remains constant at (21 ± 1) F·cm^{-3} across the

https://doi.org/10.1021/acsaelm.5c01861
ACS Appl. Electron. Mater. 2025, 7, 10998−11005

full thickness range (Figure 2a). For SE, however, a decrease in C* is observed for thicknesses above 800 nm (Figure 2b). These findings indicate that the volumetric capacitance of the film is strongly influenced by the choice of doping electrode, particularly the A_{film}/A_{Dop} ratio. Specifically, they suggest that for nonpolarizable electrodes, a high kinetic demand for ion neutralization can induce a transition toward polarizable-like behavior, limiting device performance by increasing the charge transfer resistance and introducing parasitic capacitive reactance (defined in the Supporting Information).

Although volumetric capacitance is generally regarded as an intrinsic property of the active layer, previous studies have shown that parameters such as the electrolyte composition[9,21,23] and the applied voltage[24] can also affect the measured values. This suggests that the assumption of intrinsic behavior holds true only under ideal conditions, and that comparisons between volumetric capacitance values should be made under identical experimental conditions. Furthermore, the results presented in Figure 2b introduce another parameter that should be considered, the geometry of the doping electrode, which can influence the impedances within the equivalent circuit and, in turn, impact the experimentally determined volumetric capacitance.

Figure 3a shows the charge-transfer resistance of the film (R_d) for both doping electrodes across different thicknesses. R_d decreases exponentially from approximately 35 kΩ to an average of (7 ± 1) kΩ as thickness increases, consistent with previously reported results.[7,25] As expected, R_d is independent of the doping electrode, as it depends solely on the physical and chemical properties of the polymer−electrolyte system. In contrast, the electrolyte resistance (R_s), shown in Figure 3b, is strongly dependent on the doping electrode size but independent of film thickness. For BE, the average R_s is (50 ± 10) Ω, whereas for SE it increases to (500 ± 200) Ω. This difference arises from two main reasons. First, the electrolyte resistance follows the Ohm's law,[14,26] and therefore system can be modeled as a resistor with a variable cross-sectional area (see Figure S12). In such a geometry, the resistance is given by eq 6

$$R_s = \rho \frac{d}{(A_{film} \times \pi r_{Dop})^{1/2}} \quad (6)$$

where ρ is the electrolyte resistivity, d is the distance between the gate and the channel and r_{Dop} is the radius of the doping electrode. This relation predicts that reducing the electrode radius increases R_s; for the electrode geometries used here, this contribution increases R_s by a factor of ∼8.3. Additional fluctuations are expected due to variations in d during the experiments.

The second reason can be understood using the Butler−Volmer equation: when the doping electrode area is substantially reduced, the current demand from the OMC film exceeds the electrode's capacity to neutralize ions. As a result, there is an increasing the interfacial charge-transfer resistance and ions starts to accumulate at the Ag/AgCl−electrolyte interface creating a parasitic capacitance. In the F&D model this additional interfacial impedances manifests as an apparent increase in R_s.

To decouple these two contributions, the data obtained using the small electrode were fitted with an equivalent circuit that includes an additional RC loop, to account for a polarizable behavior of the Ag/AgCl ($R_g||C_g - R_s - R_d||C_d$, for further information refer to the Supporting Information, Section S7). Here, R_g refers to the charge transfer resistance and C_g to the capacitance of the doping electrode. To constrain the fit and ensure physically meaningful values, R_d was fixed to the value obtained for the BE configuration (given that R_d must be independent of the Ag/AgCl geometry).

Figure 3c, presents the values obtained (the fits for all samples are provided in Figure S14 and Table S5). We observe that R_s yields a value lower than that obtained from the F&D model fitting, as it now represents solely the resistance predicted by Ohm's law. The obtained R_g lies in the range of few hundred ohms and shows no clear dependence on film thickness. C_g is in the order of millifarads, increasing up to ∼800 nm, plateauing afterward. We also noted that C_g is slightly larger than C_d for thin films, but became slightly smaller for thicker one (above ∼800 nm). Both transitions occur at the same point at which the volumetric capacitance decreases (Figure 2b), corroborating our hypothesis that the doping electrode undergoes a transition in operating regime toward a polarizable-like behavior. Finally, C_d is consistent with the value obtained using F&D model, resulting essentially in the same trend of volumetric capacitance versus thickness (Figure S15). This confirms that the additional impedance at the doping electrode−electrolyte interface is accounted in electrolyte resistance in the F&D model.

Due to the increase in impedance at the doping electrode−electrolyte interface, part of the applied voltage is now dropped across this interface rather than at the electrolyte−film interface - the latter being essential for driving cations into the bulk channel. Since both models yield the same conclusions, we adopt the F&D model for all subsequent analyses. For thick films tested with SE, R_s becomes comparable to R_d, leading to a substantial voltage drop across the electrolyte and consequently reducing the voltage at the electrolyte−film interface. The F&D model allows extraction of this interfacial voltage as a function of time (eq 5) and determination of the voltage across the electrolyte−film interface. Figure S6 shows the time-dependent voltage. Initially, the voltage across the film is zero, as the device perceives the applied voltage as a high-frequency pulse, with the capacitor effectively acting as a short circuit due to its low capacitive reactance (refer to the Supporting Information, Section S8). As the capacitor charges, the capacitive reactance of the film increases, producing such a voltage division. Once fully charged, the capacitor behaves as an open circuit, and the voltage division is determined by the R_d/R_s ratio.

Figure 3c shows the steady-state voltage drop across the film (V_{film}^{steady}), which was determined in the limit of $t \to \infty$, for both doping electrode configurations. For BE, V_{film}^{steady} remains constant across all devices, averaging (298 ± 1) mV—very close to the nominal applied voltage of 300 mV. In contrast, for SE, V_{film}^{steady} decreases systematically with increasing film thickness, indicating that the reduction in volumetric capacitance is linked to a diminished electrical driving force for cation injection into the film bulk. This behavior is commonly observed in OECTs with polarizable electrodes, where the double-layer capacitance at the gate reduces the voltage drop at the electrolyte−channel interface, leading to lower modulation of the drain current.[12,13,27] These results emphasize the critical role of the doping electrode in maintaining effective volumetric capacitance and highlight the importance of optimizing electrode design to ensure efficient ionic modulation in electrochemical devices. Im-

https://doi.org/10.1021/acsaelm.5c01861
ACS Appl. Electron. Mater. 2025, 7, 10998−11005

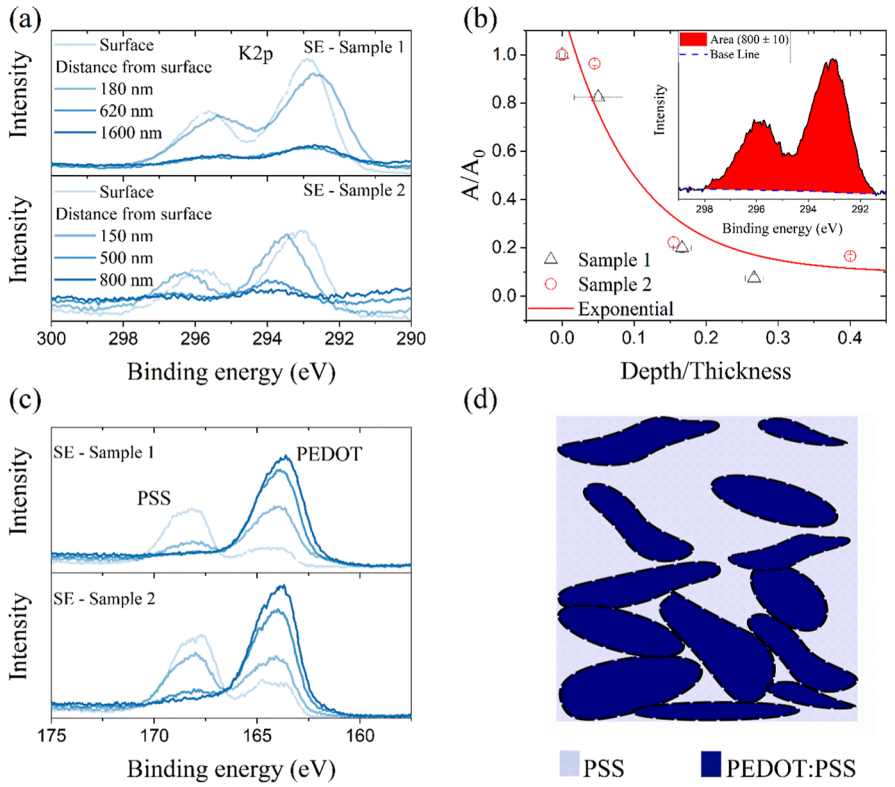

Figure 4. (a) Depth-profile XPS spectra showing K(2p) signals for thick films (2500 nm) dedoped with the SE (b) Normalized area under the curve as a function of the ratio depth/thickness. Depth is defined as the distance from the surface to the region where the spectra was obtained. Inset: Calculus of the area under the curve using the software CasaXPS. (c) Depth-profile XPS spectra showing S(2p) signals for thicker film dedoped with SE for two similar samples. (d) Illustration of the PEDOT:PSS morphology. Matrix of PSS (light blue) with aggregates of PEDOT:PSS (dark blue).

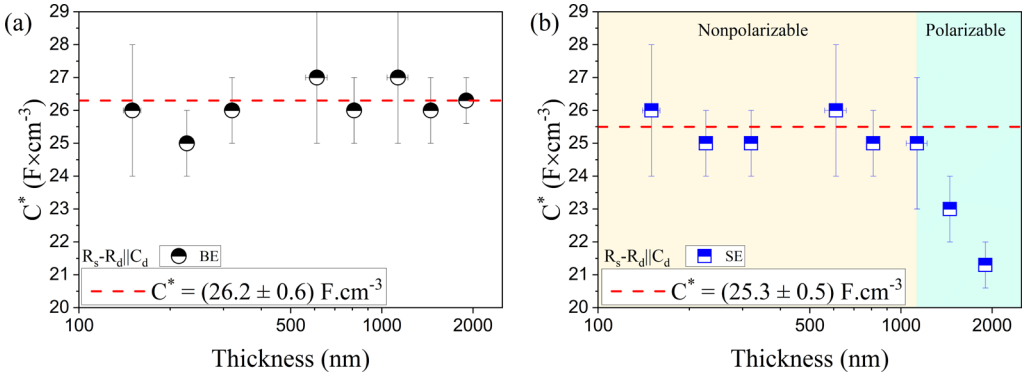

Figure 5. Volumetric capacitance for capacitor-like devices tested in 100 mM aqueous solution of $MgCl_2$. (a,b) Volumetric capacitance of each film versus thickness for BE and SE, respectively. The dashed line indicates the average volumetric capacitance. The background colors in (b) indicates the region where there is the transition from nonpolarizable to polarizable regime. The transient current data with fittings for all the samples are shown in Figures S7, and S8. The charge transfer resistance (R_d), the electrolyte resistance (R_s) and voltage on the film (V_{film}^{steady}) are shown on Figure S9.

portantly, they also demonstrate that merely using a non-polarizable electrode is not sufficient: the electrode's geometric and electrochemical properties must be carefully considered, or it may exhibit polarizable-like behavior.

To investigate the distribution of cations within the film, depth-profile X-ray photoelectron spectroscopy (XPS) was performed on thick films dedoped using SE. Samples were prepared according to the protocol described in the Materials and Methods section, which traps potassium ions within the film bulk after the system reaches steady state. Figure 4a shows the K(2p) spectra for two samples, revealing a decrease in signal intensity with depth, indicative of reduced potassium ion concentration further from the surface. To quantify this effect, the area under the K(2p) peak was calculated (inset, Figure 4b) and normalized values were plotted as a function of the depth-to-thickness ratio (Figure 4b). The results show an exponential decrease in potassium concentration, reaching approximately 80% of the surface value at the deepest regions. In contrast, thin films (150 nm) exhibit a uniform ion distribution throughout the bulk, with ion concentrations even higher than at the surface (Figure S10). These findings indicate that ions can readily permeate and occupy the entire volume in

https://doi.org/10.1021/acsaelm.5c01861
ACS Appl. Electron. Mater. 2025, 7, 10998−11005

thin films, whereas in thick films they preferentially accumulate near the surface.

The results discussed above can be related to the morphology of PEDOT:PSS. Depth-profile XPS of S(2p) (Figure 4c) reveals vertical phase separation, with a PSS-rich region near the surface and a PEDOT:PSS-rich region closer to the substrate. Combining these observations with previous literature reports,[28−30] the PEDOT:PSS morphology can be represented as a PSS matrix interspersed with PEDOT:PSS agglomerates, whose concentration increases toward the bottom of the film (Figure 4d). It is well established that water-hydrated ions are transported more efficiently within the PSS-rich phase[28,29,31,32] due to its amorphous, hydrophilic nature, which offers lower impedance compared to the more crystalline PEDOT regions. When ions penetrate the denser, PEDOT:PSS-rich regions, they must either shed part of their hydration shell[23] or be driven by a sufficiently strong electric field,[33] both energetically demanding processes. Consequently, in systems using SE and thick PEDOT:PSS films - where a significant voltage drop occurs across the Ag/AgCl−electrolyte interface - there is insufficient energy to drive ions throughout the full film volume. This limited ion penetration results in a reduction of the effective volumetric capacitance.

The volumetric capacitance of OMCs has been shown to depend on the ionic species present in the electrolyte.[21,23,34] To assess whether the ionic species also influence the limit of the linear relationship between capacitance and thickness/volume, we repeated the electrical measurements on a new batch of devices using an aqueous $MgCl_2$ solution as the electrolyte. Devices tested with $MgCl_2$ exhibited similar trends (Figure 5). For BE, the volumetric capacitance remained constant across the entire thickness range, averaging 26 F·cm^{-3}. For SE, deviation from linearity was observed for thicknesses above 1000 nm (volume ≈ 1.425 × 10^6 μm^3). These results are consistent with our previous work,[21] which showed that PEDOT:PSS-based OECTs exhibit higher volumetric capacitance when operated in $MgCl_2$ compared to KCl. This behavior is attributed to the superior ability of Mg^{2+} cations to swell the PEDOT:PSS film. In the present case, the enhanced hydration of PEDOT:PSS by Mg^{2+}, combined with its smaller ionic radius relative to K^+, contributes to extending the linear range of the capacitance−thickness/volume relationship.

CONCLUSIONS

Our findings demonstrate that volumetric capacitance is not solely determined by the combination of the active layer material and the electrolyte, but is also strongly influenced by the choice of doping electrode. Transient measurements on PEDOT:PSS-based capacitor-like devices, analyzed using the F&D model, revealed a threshold beyond which the capacitance of OMC films no longer scales linearly with volume. Depth-profile XPS further showed that, for films exceeding this volume, the ion concentration decreases with depth, whereas in smaller-volume films it remains uniform. This deviation originates from an increasing voltage drop at the Ag/AgCl-electrolyte interface, a behavior inconsistent with ideal nonpolarizable electrode operation. According to the Butler−Volmer equation, this indicates a transition toward polarizable-like behavior. Our study highlights that the surface area of the Ag/AgCl doping electrode must be appropriately matched to the OMC film and electrolyte properties to preserve nonpolarizable behavior. These results provide critical insights into the factors governing volumetric capacitance in OMCs and underscore the limitations of standard Ag/AgCl pellets commonly used in electrochemical device fabrication.

ASSOCIATED CONTENT

Supporting Information

The Supporting Information is available free of charge at https://pubs.acs.org/doi/10.1021/acsaelm.5c01861.

Includes a sketch of the sample structure, a profilometry graphic, all transient curves along with their corresponding fits using the Faria & Duong (F&D) model and the equivalent circuit $R_g||C_g - R_s - R_d||C_d$, accompanied by tables summarizing the extracted fitting parameters. Additionally, complementary depth-profile X-ray Photoelectron Spectroscopy (XPS) results are provided (PDF)

AUTHOR INFORMATION

Corresponding Authors

Renan Colucci − *Instituto de Física de São Carlos, Universidade de São Paulo, São Carlos, São Paulo 13566-590, Brazil;* Present Address: Organic Bioelectronics Research Group, Max Planck Institute for Polymer Research, Ackermannweg 10, 55128 Mainz, Germany; orcid.org/0000-0002-0669-9823; Email: coluccir@mpip-mainz.mpg.de

Gregório Couto Faria − *Instituto de Física de São Carlos, Universidade de São Paulo, São Carlos, São Paulo 13566-590, Brazil;* orcid.org/0000-0001-6138-8473; Email: gcfaria@ifsc.usp.br

Authors

Paula Cristina Rodrigues − *Departamento de Química e Biologia, Universidade Tecnológica Federal do Paraná, Curitiba, Paraná 81280-340, Brazil;* orcid.org/0000-0002-9712-6149

Rafael Francisco Santiago de Souza − *Instituto de Física de São Carlos, Universidade de São Paulo, São Carlos, São Paulo 13566-590, Brazil*

Complete contact information is available at: https://pubs.acs.org/10.1021/acsaelm.5c01861

Author Contributions

R.C.: conceptualization, methodology, carried out experiments, data analysis, writing-original draft. G.C.F.: conceptualization, supervision, data analysis, funding acquisition, writing-original draft. P.C.R and R.F.S.S.: data analysis (Butler−Volmer). All authors have given approval to the final version of the manuscript.

Funding

This study was financed in part by the Coordenação de Aperfeiçoamento de Pessoal de Nível Superior—Brasil (CAPES)—Finance Code 001, by INCT/FAPESP/CNPq INEO Project (grant. no 2014/50869-6) and by Conselho Nacional de Desenvolvimento Científico e Tecnológico (CNPq), grant no 308985/2025-7. The Article Processing Charge for the publication of this research was funded by the Coordenacao de Aperfeicoamento de Pessoal de Nivel Superior (CAPES), Brazil (ROR identifier: 00x0ma614).

Notes

The authors declare no competing financial interest.

■ ACKNOWLEDGMENTS

The authors would like to thank Prof. Dr. Renato Vitalino Gonçalves from the Laboratory of Nanomaterials and Advanced Ceramics (NaCA—IFSC/USP) for his assistance in the XPS characterization.

■ ABBREVIATIONS

OMC, organic mixed conductor; PEDOT:PSS, poly(3,4-ethylenedioxythiophene):poly(styrenesulfonate); Ag/AgCl, silver/silver chloride; F&D, Faria-Duong; XPS, X-ray photoelectron spectroscopy.

■ REFERENCES

(1) Keene, S. T.; Gueskine, V.; Berggren, M.; Malliaras, G. G.; Tybrandt, K.; Zozoulenko, I. Exploiting Mixed Conducting Polymers in Organic and Bioelectronic Devices. *Phys. Chem. Chem. Phys.* **2022**, *24*, 19144−19163.
(2) Gkoupidenis, P.; Zhang, Y.; Kleemann, H.; Ling, H.; Santoro, F.; Fabiano, S.; Salleo, A.; van de Burgt, Y. Organic Mixed Conductors for Bioinspired Electronics. *Nat. Rev. Mater.* **2024**, *9* (2), 134−149.
(3) Kim, H.; Won, Y.; Song, H. W.; Kwon, Y.; Jun, M.; Oh, J. H. Organic Mixed Ionic−Electronic Conductors for Bioelectronic Sensors: Materials and Operation Mechanisms. *Advanced Science* **2024**, *11* (27), 1−28.
(4) Paulsen, B. D.; Tybrandt, K.; Stavrinidou, E.; Rivnay, J. Organic Mixed Ionic−Electronic Conductors. *Nat. Mater.* **2020**, *19*, 13−26.
(5) Wu, R.; Matta, M.; Paulsen, B. D.; Rivnay, J. Operando Characterization of Organic Mixed Ionic/Electronic Conducting Materials. *Chem. Rev.* **2022**, *122*, 4493−4551.
(6) Proctor, C. M.; Rivnay, J.; Malliaras, G. G. Understanding Volumetric Capacitance in Conducting Polymers. *J. Polym. Sci. Part B: Polym. Phys.* **2016**, *54*, 1433−1436.
(7) Rivnay, J.; Leleux, P.; Ferro, M.; Sessolo, M.; Williamson, A.; Koutsouras, D. A.; Khodagholy, D.; Ramuz, M.; Strakosas, X.; Owens, R. M.; Benar, C.; Badier, J.-M. J.-M.; Bernard, C.; Malliaras, G. G. High-Performance Transistors for Bioelectronics through Tuning of Channel Thickness. *Sci. Adv.* **2015**, *1* (4), No. e1400251.
(8) Savva, A.; Hallani, R.; Cendra, C.; Surgailis, J.; Hidalgo, T. C.; Wustoni, S.; Sheelamanthula, R.; Chen, X.; Kirkus, M.; Giovannitti, A.; Salleo, A.; McCulloch, I.; Inal, S. Balancing Ionic and Electronic Conduction for High-Performance Organic Electrochemical Transistors. *Adv. Funct. Mater.* **2020**, *30* (11), 1−9.
(9) Coutinho, D. J.; de Andrade Feitosa, B.; de Paula Barbosa, H. F.; Colucci, R.; Torres, B. B. M.; Faria, G. C. Distinctive Behavior of Field-Effect and Redox Electrolyte-Gated Organic Transistors. *J. Phys. Chem. C* **2023**, *127* (50), 24443−24451.
(10) Dreamer, N. E.; Koutsouras, D. A.; Hassanpour Amiri, M.; Gkoupidenis, P.; Asadi, K. The Impact of Non-Monolithic Semiconductor Capacitance on Organic Electrochemical Transistors Performance and Design. *Adv. Electron Mater.* **2024**, *10*, 2400373.
(11) Bianchi, M.; Carli, S.; Di Lauro, M.; Prato, M.; Murgia, M.; Fadiga, L.; Biscarini, F. Scaling of Capacitance of PEDOT:PSS: Volume: Vs. Area. *J. Mater. Chem. C* **2020**, *8* (32), 11252−11262.
(12) Rivnay, J.; Inal, S.; Salleo, A.; Owens, R. M.; Berggren, M.; Malliaras, G. G. Organic Electrochemical Transistors. *Nat. Rev. Mater.* **2018**, *3* (2), 17086.
(13) Ohayon, D.; Druet, V.; Inal, S. A Guide for the Characterization of Organic Electrochemical Transistors and Channel Materials. *Chem. Soc. Rev.* **2023**, *52*, 1001−1023.
(14) Bard, A. J.; Faulkner, L. R. *Electrochemical Methods: Fundamentals and Applications*; John Wiley & Sons, Inc, 2004.
(15) Brown, R. J. C.; Brewer, P. J.; Brett, D. J. L. Long-Term Equilibrium Potential and Electrochemical Impedance Study of Ag/AgCl Electrodes Used in Harned Cell Measurements of PH. *Accredit. Qual. Assur.* **2009**, *14* (3), 139.
(16) Dickinson, E. J. F.; Wain, A. J. The Butler-Volmer Equation in Electrochemical Theory: Origins, Value, and Practical Application. *J. Electroanal. Chem.* **2020**, *872*, 114145.
(17) Fletcher, S. Butler−Volmer Meets Microscopic Reversibility. *Curr. Opin. Electrochem.* **2023**, *37*, 101199.
(18) Gu, H.; Bennion, D. N. Diffusion and Charge Transfer Parameters for the Ag/AgCl Electrode. *J. Electrochem. Soc.* **1977**, *124* (9), 1364.
(19) Faria, G. C.; Duong, D. T.; Salleo, A. On the Transient Response of Organic Electrochemical Transistors. *Org. Electron.* **2017**, *45*, 215−221.
(20) Duc, C.; Vlandas, A.; Malliaras, G. G.; Senez, V. Wettability of PEDOT:PSS Films. *Soft Matter* **2016**, *12* (23), 5146−5153.
(21) Colucci, R.; Feitosa, B. d. A.; Faria, G. C. Impact of Ionic Species on the Performance of Pedot:PSS-Based Organic Electrochemical Transistors. *Adv. Electron Mater.* **2024**, *10* (2), 1−8.
(22) Huang, Y.; Tang, L.; Jiang, Y. Chemical Strategies of Tailoring PEDOT:PSS for Bioelectronic Applications: Synthesis, Processing and Device Fabrication. *CCS Chem.* **2024**, *6*, 1844−1867.
(23) Cendra, C.; Giovannitti, A.; Savva, A.; Venkatraman, V.; McCulloch, I.; Salleo, A.; Inal, S.; Rivnay, J. Role of the Anion on the Transport and Structure of Organic Mixed Conductors. *Adv. Funct. Mater.* **2019**, *29* (5), 1−11.
(24) Luginieski, M.; Torres, B. B. M.; Faria, G. C. Guidelines on Measuring Volumetric Capacitance in Organic Electrochemical Transistors. *ACS Appl. Electron. Mater.* **2024**, *6* (4), 2225−2231.
(25) Colucci, R.; Barbosa, H. F. D. P.; Günther, F.; Cavassin, P.; Faria, G. C. Recent Advances in Modeling Organic Electrochemical Transistors. *Flexible Printed Electron.* **2020**, *5* (1), 013001.
(26) Koutsouras, D. A.; Amiri, M. H.; Blom, P. W. M.; Torricelli, F.; Asadi, K.; Gkoupidenis, P. An Iontronic Multiplexer Based on Spatiotemporal Dynamics of Multiterminal Organic Electrochemical Transistors. *Adv. Funct. Mater.* **2021**, *31* (22), 2011013.
(27) Zhao, C.; Yang, J.; Ma, W. Transient Response and Ionic Dynamics in Organic Electrochemical Transistors. *Nano-Micro Lett.* **2024**, *16*, 233.
(28) Stavrinidou, E.; Leleux, P.; Rajaona, H.; Khodagholy, D.; Rivnay, J.; Lindau, M.; Sanaur, S.; Malliaras, G. G. Direct Measurement of Ion Mobility in a Conducting Polymer. *Adv. Mater.* **2013**, *25* (32), 4488−4493.
(29) Rivnay, J.; Inal, S.; Collins, B. A.; Sessolo, M.; Stavrinidou, E.; Strakosas, X.; Tassone, C.; Delongchamp, D. M.; Malliaras, G. G. Structural Control of Mixed Ionic and Electronic Transport in Conducting Polymers. *Nat. Commun.* **2016**, *7*, 11287.
(30) Volkov, A. V.; Wijeratne, K.; Mitraka, E.; Ail, U.; Zhao, D.; Tybrandt, K.; Andreasen, J. W.; Berggren, M.; Crispin, X.; Zozoulenko, I. V. Understanding the Capacitance of PEDOT:PSS. *Adv. Funct. Mater.* **2017**, *27* (28), 1700329.
(31) Savva, A.; Wustoni, S.; Inal, S. Ionic-to-Electronic Coupling Efficiency in PEDOT:PSS Films Operated in Aqueous Electrolytes. *J. Mater. Chem. C* **2018**, *6* (44), 12023−12030.
(32) Wu, R.; Ji, X.; Ma, Q.; Paulsen, B. D.; Tropp, J.; Rivnay, J. Direct Quantification of Ion Composition and Mobility in Organic Mixed Ionic-Electronic Conductors. *Sci. Adv.* **2024**, *10*, 8628.
(33) Guardado, J. O.; Salleo, A. Structural Effects of Gating Poly(3-Hexylthiophene) through an Ionic Liquid. *Adv. Funct. Mater.* **2017**, *27* (32), 1701791.
(34) Flagg, L. Q.; Giridharagopal, R.; Guo, J.; Ginger, D. S. Anion-Dependent Doping and Charge Transport in Organic Electrochemical Transistors. *Chem. Mater.* **2018**, *30* (15), 5380−5389.

https://doi.org/10.1021/acsaelm.5c01861
ACS Appl. Electron. Mater. 2025, 7, 10998−11005